PHOTONICS Research

Plasmon resonance-enhanced graphene nanofilm-based dual-band infrared silicon photodetector

Xinyu Liu,[1] Shaoxiong Wu,[1,2] Xiaoxue Cao,[1,3] Feng Tian,[1,2] Srikrishna Chanakya Bodepudi,[1] Muhammad Malik,[1] Chao Gao,[3] Li Peng,[1,4] Huan Hu,[2,5] and Yang Xu[1,2,6]

[1]School of Micro-Nano Electronics, ZJU-Hangzhou Global Scientific and Technological Innovation Center, State Key Laboratory of Silicon and Advanced Semiconductor Materials, Zhejiang University, Hangzhou 310027, China
[2]ZJU-UIUC Institute, International Campus, Zhejiang University, Haining 314400, China
[3]Department of Polymer Science and Engineering, MOE Key Laboratory of Macromolecular Synthesis and Functionalization, Key Laboratory of Adsorption and Separation Materials & Technologies of Zhejiang Province, Zhejiang University, Hangzhou 310027, China
[4]e-mail: l-peng@zju.edu.cn
[5]e-mail: huanhu@intl.zju.edu.cn
[6]e-mail: yangxu-isee@zju.edu.cn

Received 31 May 2023; revised 30 July 2023; accepted 30 July 2023; posted 31 July 2023 (Doc. ID 496848); published 21 September 2023

Graphene-based photodetectors have attracted much attention due to their unique properties, such as high-speed and wide-band detection capability. However, they suffer from very low external quantum efficiency in the infrared (IR) region and lack spectral selectivity. Here, we construct a plasmon-enhanced macro-assembled graphene nanofilm (nMAG) based dual-band infrared silicon photodetector. The Au plasmonic nanostructures improve the absorption of long-wavelength photons with energy levels below the Schottky barrier (between metal and Si) and enhance the interface transport of electrons. Combined with the strong photo-thermionic emission (PTI) effect of nMAG, the nMAG–Au–Si heterojunctions show strong dual-band detection capability with responsivities of 52.9 mA/W at 1342 nm and 10.72 mA/W at 1850 nm, outperforming IR detectors without plasmonic nanostructures by 58–4562 times. The synergy between plasmon–exciton resonance enhancement and the PTI effect opens a new avenue for invisible light detection.

https://doi.org/10.1364/PRJ.496848

1. INTRODUCTION

Graphene, single-layer carbon material with zero band gap, is a promising material for future electronic [1–3] and optoelectronic [4–9] applications owing to its exceptional combination of several significant characteristics [7–20], such as excellent flexibility [10–12] and high carrier mobility [19,20]. Graphene-based photodetectors can be used in broadband (300 nm to 4.2 μm) applications [14–18,21,22]. Characterized by robust electron–electron interaction and weak electron–phonon coupling [23,24], graphene exhibits rapid thermalization within the electron system [25–29] (approximately 50 fs) prior to thermal equilibrium with the lattice in several picoseconds. Therefore, graphene-based heterostructures show great potential for detecting and utilizing photons with energies slightly below the Schottky barrier [30–32] due to graphene's photo-thermionic emission (PTI) effect. Nevertheless, the performance of graphene-based IR photodetectors is constrained by monolayer graphene's light absorption capability (~2.3%) [33,34] and relatively weak PTI effect.

Recently, our group proposed macro-assembled graphene nanofilms (nMAGs). They demonstrate uniform and controllable thickness, high-quality crystal lattice, and zero band gap structure. The bulk structure and AB-stacked configuration endow the nMAG with a high absorption (~40%) within the infrared wavelength range, a long carrier relaxation time (~4.9 ps), and hence a more robust PTI effect [35–37] than that of monolayer graphene [36]. Nevertheless, the quantum efficiency (QE) of graphene-based heterojunctions is still not up to the minimum application requirements. Besides, nMAGs have a broadband absorption spectrum, precluding their application in spectral selectivity.

Localized surface plasmon resonance (LSPR) occurs when the incident light frequency matches the free electrons' oscillation frequency in a designed metallic nanostructure. This phenomenon results in the generation of surface plasmons at the metallic–dielectric interface and generates an intense and highly localized electromagnetic field [38–42]. This property has been widely exploited to enhance the QE [43,44]. In the infrared range, metallic nanostructures are also integrated with semiconductor detectors to enhance photon absorption and improve carrier transport efficiency [45–47]. Moreover, surface plasmon polaritons coupled to the graphene surface demonstrate unique features such as high modal indices, relatively low loss, and flexible tunability through electric and magnetic fields [48–50].

To surmount the limitations posed by the monolayer graphene absorption and attain the practical benefits of graphene-based photodetectors, a new approach is presented in this study for constructing highly sensitive dual-band photodetectors. This approach integrates the localized electric field generated from metallic plasmonic nanostructure with the unique absorption characteristics and strong PTI effects of nMAG. Plasmonic nanostructures composed of metal on the top and bottom surfaces of silicon cylinders can enhance optical detection and photoresponse at specific plasmon resonance frequencies, thereby enabling sensitive responses from a dual-band of 1342 nm and 1850 nm in nMAG–Au–Si photodetectors. Photoresponse studies show that integrating the plasmonic nanostructure can significantly improve photocurrent up to 5800%, achieving a responsivity of 52.9 mA/W and a detectivity of 4.77×10^{10} Jones. Implementing this dual-band detector provides a new approach to surpass the performance limitations of traditional silicon-based infrared photodetectors.

2. EXPERIMENTAL SECTION

A. Device Fabrication

Figure 1(a) presents the schematic illustration of the procedural flow used to couple plasmonic nanostructures with an nMAG photodetector. The process involves cleaning a standard n-type silicon wafer substrate (500 μm thickness, 1–10 Ω · cm resistivity) with acetone and isopropanol in an ultrasonic bath for 5 min, followed by drying with N_2. A silicon window was patterned using photolithography and buffered oxide etchant (BOE). The photoresist is left outside the silicon window area as a mask.

First, a 5-min oxygen plasma treatment (Diener, ZEPTO RIE) was used to render the silicon window area surface hydrophilic, employing a power of 240 W and an O_2 pressure of 0.4 mbar (1 mbar = 100 Pa). Next, we applied a mixture of propylene glycol and carboxyl-modified polystyrene nanospheres with 1 μm diameter (Beijing Zhongkeleiming, 10% by weight) in a volume ratio of 3:2. We then applied a 100 μL droplet of the mixture on one corner in the Si window. At the same time, pure water filled the rest of the substrate. Due to the Marangoni effect [51,52] at the water boundary, the droplet self-assembled into a monolayer of polystyrene nanospheres on the water surface. After 8 min, we used absorbent paper to slowly remove the water from underneath the monolayer. Finally, we heated the devices on a hot plate at 60°C for 10 min to enhance the adhesion.

To decrease the size of the nanospheres [53], a monolayer of polystyrene nanospheres was placed on Si substrate and subjected to O_2 plasma etching for 2 min with a power of 180 W and an oxygen pressure of 0.4 mbar. The silicon

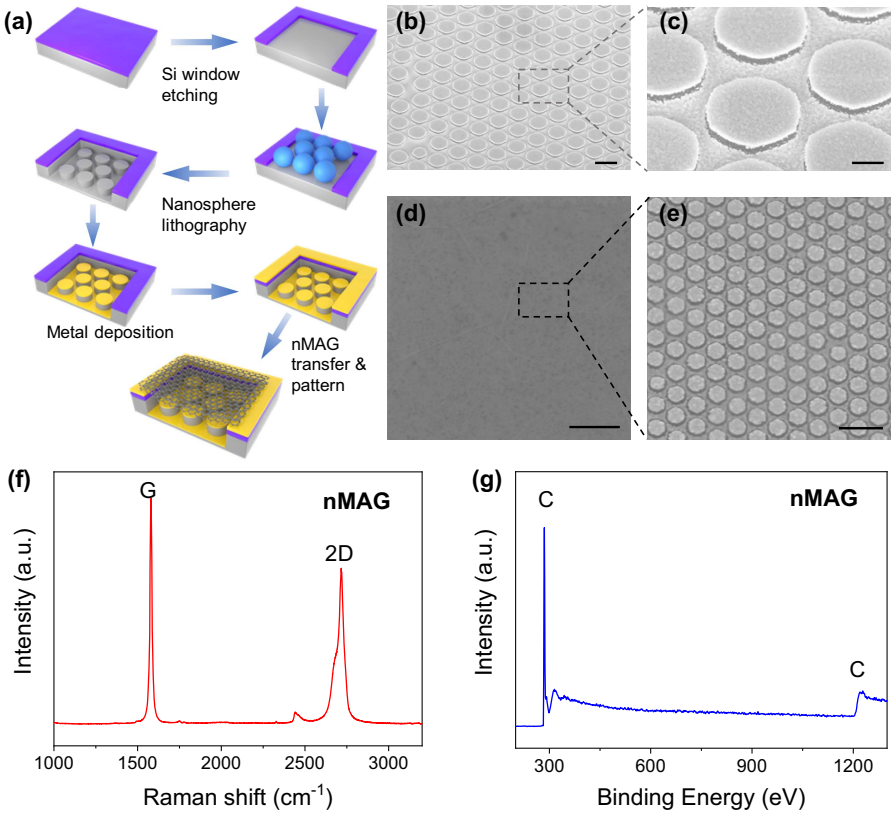

Fig. 1. Plasmonic-enhanced nMAG–Au–Si nanostructure architecture. (a) Schematic of the nMAG–Au–Si nanostructure fabrication process using the nanosphere lithography method. (b), (c) Oblique view SEM images of the Si cylinder with the metallic nanostructure. The top–bottom metallic layer was deposited by 3 nm Ti and 30 nm Au. (d) Top view SEM image of the nMAG transferred on the metallic nanostructures. (e) Close-up SEM image of the area outlined by the dashed box in panel (d) shows the metallic coupled plasmon covered by nMAG film. The scale bars are 1 μm, 300 nm, 100 μm, and 2 μm in panels (b)–(e), respectively. (f) Raman spectrum of nMAG. (g) X-ray photoelectron spectroscopy (XPS) profile of the nMAG with no detectable oxygen peak (531.5 eV). C represents the carbon peak.

substrate was subsequently etched utilizing the reactive gases of CHF_3 and SF_6 (gas flow: 45:13 sccm) for 2 min with a pressure of 0.5 Pa, using the reduced nanosphere monolayer as a mask. The inductively coupled plasma and radio frequency powers applied from inductively coupled plasma (ICP, Sentech, type SI 500) were set at 100 and 5 W, respectively. Following etching, the remaining nanosphere monolayer was cleaned in an ultrasonic bath with 1,1,2-trichlorotrifluoroethane (AR, 99%). Subsequently, the devices were evaporated (Sky Technology, DZS-500) with the Ti/Au (3 nm/30 nm) layer as a plasmonic substrate. Finally, the Ti/Au (15 nm/30 nm) contacts were formed as electrodes through ultraviolet lithography and e-beam evaporation and were then subjected to a lift-off process.

Next, the devices were placed in acetone and isopropanol to remove the photoresist. Then the distilled water was used to fulfill the gap between the nMAG and the Si window/electrodes. The surface tension of water helps unfold the nMAG and smooth this film on the silicon. High-pressure N_2 purged on nMAG to remove the water, leaving a flat film on the substrate. Photolithography further patterned the device to etch the extra part of nMAG outside the electrodes by the ICP dry etching system (OXFORD, Plasmapro100 Cobra 180). Afterward, the rapid thermal process (RTP) was used to perform good contact by applying the annealing process of 400°C for 5 min. Finally, GaIn obtained ohmic contact at the back side of the silicon, and wire bonding was performed to connect the device with the designed printed circuit board (PCB).

B. Materials and Device Characterization

Raman spectra were acquired using a Renishaw in Via-Reflex Raman microscope (laser source, 532 nm). A scanning electron microscopy (SEM) image was obtained from a Hitachi S4800 field emission system. XPS was performed with a Thermo Scientific K-Alpha System operated at 12.0 kV.

Fourier-transform infrared (FTIR) spectroscopy was implemented using a Bruker Hyperion 1000 IR microscope (15-fold magnification, NA = 0.4) coupled with a Bruker Vertex 70 spectrometer. A 200-nm-thick flat Au film was used as a reference in the reflection measurement.

The electrical measurements were performed by a Tektronix Source Measure Unit 2450. The continuous lasers provided near-infrared (NIR) light with wavelengths of 1342 nm and 1850 nm. The power of the laser source was measured by an optical power meter in InGaAs (Thorlabs S184C) photodetectors. For the time-dependent response measurement, the device was connected with the trans-impedance amplifier (TIA, DHPCA-100, FEMTO, 200 MHz bandwidth) and an oscilloscope (Agilent DSO 9404A, 4 GHz bandwidth). The laser was modulated by a signal generator (RIGOL DG 2302, 200 MHz bandwidth) to generate a TTL signal. A noise measurement system (PDA NC300L, 100 kHz bandwidth) recorded the noise power spectra, which could apply various bias voltages to the device.

C. Ultrafast Transient Absorption Measurement

Femtosecond transient absorption experiments were conducted using a Yb:KGW laser system (PHAROS, Light Conversion Ltd.) with a fundamental output wavelength of 1030 nm, pulse duration of <190 fs, energy of 200 μJ/pulse, and a repetition rate of 100 kHz. Nonlinear frequency mixing techniques and the Femto-TA100 spectrometer (Time-tech Spectra) were utilized. The laser output is split using a beam splitter into two beams of different intensities. The stronger beam pumps an optical parametric amplifier (OPA, Orpheus-HP, Light Conversion Ltd.), equipped with deference frequency generation (DFG) to generate a probe beam at the NIR region. The weaker beam is used as the probe. The pump beam passes through a chopper and a focusing mirror, while the probe beam is sent through an optical delay line. The delay line controls the time delay between the pump and probe beams. The probe beam is then focused onto the sample, and the transmitted beam is detected at a frequency of 10 kHz by a fiber-coupled spectrometer with a CMOS sensor.

D. Simulation

The electric field distribution was simulated using the commercial software COMSOL Multiphysics v5.6 to numerically solve Maxwell's equations under a typical incident IR light.

3. RESULTS AND DISCUSSION

A. Properties Characterization of Device and nMAG

Figure 1 illustrates the schematic representation of the preparation procedure for the plasmonic resonance-enhanced photodetector. Initially, Si was etched into Si cylinders using the nanosphere lithography technique described in device fabrication. Next, the plasmonic nanostructure was fabricated with the LSPR effect by employing e-beam deposition to deposit the metal layer (3 nm Ti/30 nm Au) on the top and bottom of the Si cylinder, utilizing the Si cylinder as a mask. The Ti layer served as an adhesion layer. The resulting Au–Si cylinder nanostructures, displaying a hexagonal arrangement with dimensions of 210 nm in height and periodicity of 1000 nm, are depicted in Figs. 1(b) and 1(c), elucidating its structural characteristics.

Subsequently, nMAG was transferred to the Au–Si cylinder nanostructure. Figure 1(d) reveals the smooth surface of the nMAG, devoid of any discernible localized depressions and wrinkles. Upon closer examination [Fig. 1(e)], the structures of the silicon cylinder become discernible. Notably, nMAG demonstrates a single-crystal graphite-like lattice structure. The undetectable D peak (1358.9 cm^{-1}) in the Raman spectrum [Fig. 1(f)] and absence of oxygen peaks (531.5 eV) in the XPS profile [Fig. 1(g)] demonstrate an in-plane lattice structure of graphene without oxygen-containing functional groups. Besides, the graphite-like 2D peak (2720 cm^{-1}) in Raman indicates an AB-stacking configuration of nMAG [Fig. 1(f)] [35].

B. Structural Characterization of the Dual-Band IR Photodetector

Figure 2(a) shows the schematic device structure of the nMAG–Au–Si vertical structure. The free-standing nMAG layer (~30 nm) covers the metallic nanostructure on the Si window (500 μm × 500 μm). Distinguished by the energy level relative to the Schottky barrier height (SBH), the higher-energy incident light is symbolized by orange rays, whereas pink rays denote the lower-energy incident light.

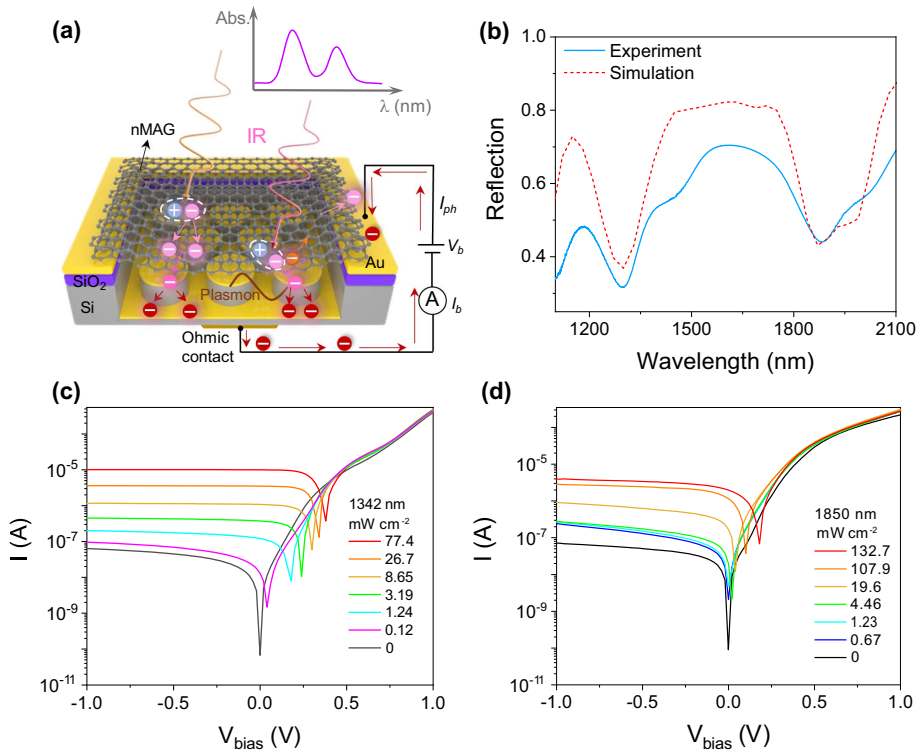

Fig. 2. Device structural characterization of the dual-band IR photodetector. (a) Schematic of the nMAG–Au–Si device showing the charge transport and the surface plasmon polariton coupled to the nMAG. The top schematic diagram shows the absorbance of the dual-band photodetector. (b) Wavelength-dependent properties of experimental (solid blue line) and simulated (red dashed line) reflection spectra. (c), (d) Current as a function of the bias voltage under laser illumination at 1342 nm and 1850 nm under different excitation power, respectively.

With the applied bias, the electrons within the nMAG experience an ultrafast thermalization process, which means that high-energy electrons will be formed at the end of the thermal distribution of nMAG (indicated by rose red electrons and arrows in the figure). The hot electrons obey the Fermi–Dirac distribution. Then these electrons tunnel into Au nanostructures. The hot electrons at Au nanostructures' interfaces and the tunneling electrons undergo further heating by the surface plasmon resonances, leading to the generation of hot electrons (indicated by the crimson color). The energy of these electrons surpasses the SBH formed by the Au–Si Schottky junction, enabling them with sufficient energy to surmount the barrier and ultimately transport to the silicon substrate. These electrons can be captured through the external circuit, contributing to the device's photocurrent.

Additionally, the plasmon-induced LSPR effect in the nanostructure contributes to near-field light trapping, which ultimately enhances absorption. The resonance wavelength of the plasmonic-enhanced structure with a period of 1000 nm is demonstrated in Fig. 2(b). The duty cycle, determined by the ratio of the width (~800 nm) to the period, is calculated to be 80%. We simulated the reflection spectrum of our photodetector by the 2D finite-element method (red dashed line) in Fig. 2(b). The absorbance could be derived according to the relationship between the absorbance (A) and reflection (R) as given by $A=1-R$. We experimentally measured the reflection of the device and confirmed the presence of two resonance peaks, which is fairly close to the simulation result. The device exhibits a dual-band absorbance of 69% and 55.9% at the wavelengths of 1340 nm and 1855 nm, respectively, attributed to the plasmon-induced light trapping. The slightly diminished values observed in the FTIR spectroscopy results for other bands, apart from the reflection peak, can be attributed to light absorption by defects at the device's interface [54].

Based on the strong light absorbance and the experimental conditions, we chose the 1342 nm and 1850 nm wavelengths typical continuous wave (CW) lasers as the light source. Figures 2(c) and 2(d) show the current-bias voltage (I-V) characteristic of the plasmon-enhanced photodetector at 1342 nm and 1850 nm with varying incident power. The rectification ratio is 6.2×10^3 at ±1 V, demonstrating the Schottky junction between the metal and n-type silicon. The SBH can be extracted by considering the thermionic emission model and diffusion of the photo-carrier [55,56] by using the following formulas:

$$I = A_{\text{eff}}A^{*}T^{2}\exp\left(\frac{-q\phi_B}{k_BT}\right)\left[\exp\frac{q(V-\text{IR})}{nk_BT}-1\right], \quad (1)$$

$$\frac{\mathrm{d}V}{\mathrm{d}\ln I} = RI + \frac{nk_BT}{q}, \quad (2)$$

$$H(I) = V - \frac{nk_BT}{q}\ln\left(\frac{I}{A_{\text{eff}}A^{*}T^{2}}\right), \quad (3)$$

$$H(I) = RI + n\phi_B, \tag{4}$$

where A_{eff} is the effective area of the device, A^* is the Richardson constant, T is the temperature, k_B is the Boltzmann constant, ϕ_B is the SBH, n is the ideal factor, and R is the series resistance. Notably, the series resistance signifies that under forward bias conditions of the Schottky diode, the presence of the SBH disrupts the linear relationship between current and voltage. Therefore, the SBH, n, and R are extracted to be 0.87 eV, 1.7, and 360 Ω, respectively, from the I-V characteristic in the dark condition.

C. Optoelectric Characteristics and Mechanism of the Plasmonic Nanostructure-Based Photodetector

Figures 3(a)–3(d) represent the normalized electric field based on device structure under 1175, 1342, 1850, and 1990 nm illumination. The red region displays a remarkably intense electric field, primarily concentrated at the interface of the plasmonic nanostructure and the vertically coupled region between the Au plasmonic structures. Additionally, enhanced electric fields are also present in the Si semiconductor region close to the Au nanostructures. The most pronounced electric field intensity of the Au nanostructures is observed around 1342 nm and 1850 nm, corresponding to the absorption peaks observed in the FTIR measurements. The simulations indicate that the enhancement of the electric field distribution at 1342 nm and 1850 nm can be primarily attributed to the following factors. First, the angular features formed by the sidewalls of the silicon cylinder result in the generation of a dipolar plasmonic resonance effect at the interface between the upper layer of the nMAG coupled with Au nanostructures and the surrounding air. The bound states of plasmon waves at the boundaries of the nanostructures lead to localized field enhancement, where the electric field accumulates and exhibits nonuniformity. These regions with significantly amplified electric fields contribute to additional absorption enhancement. Second, the coupling effect between the lower surface of the upper Au nanostructure and the silicon cylinder gives rise to the LSPR effect. Near the silicon cylinder interface at 1850 nm, the strongest field enhancement is observed. This plasmonic enhancement effect is associated with wavelength-dependent resonance. Lastly, the enhanced electric field due to the LSPR effect occurring at the interface between the lower Au nanostructure and the silicon pillar can be observed.

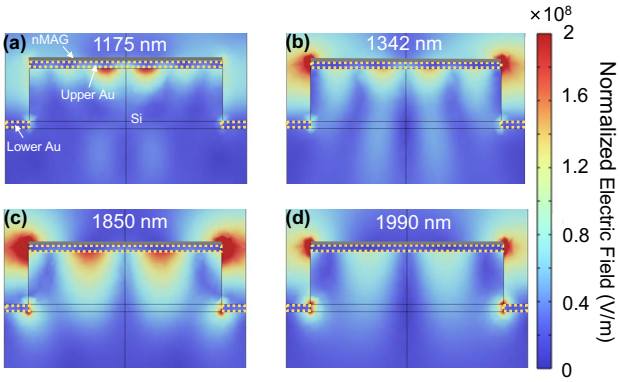

Fig. 3. Mechanism for the enhancement electric field of the nMAG–Au–Si photodetector. (a)–(d) Simulated electric field distribution of the nanostructure-based device under illumination with the wavelengths of 1175, 1342, 1850, and 1990 nm, respectively.

The Au thin film deposited on the Si nanocylinder can introduce the surface plasmon resonance effect. This surface plasmon nanostructure in the nMAG–Au–Si device primarily serves two enhancement effects: on one hand, it achieves the localization and enhancement of the optical field; on the other hand, through nonradiative relaxation mechanisms such as Landau damping [57], it directly excites thermal charge carriers by transferring energy to the electronic system [44,46,58,59]. In terms of the localization and enhancement of the optical field, it mainly stems from the near-field oscillation and scattering effects of the Au nanostructures [60,61]. First, when the localized surface plasmons of the Au nanostructures are excited by electromagnetic radiation at specific frequencies, electronic oscillations occur within the Au nanostructures. Through these oscillations, light is confined and effectively constrained and amplified around the surface of the Au nanostructures, significantly enhancing the local optical field and improving the light absorption efficiency of the devices within specific wavelength ranges. Second, the scattering effect of the Au nanostructures' surface plasmons contributes to the enhancement of photocurrent. The scattering interaction between the Au nanostructures' plasmonic excitons and neighboring Au nanostructures leads to strong coupling between the nanostructures. This coupling captures light within the nanostructure array plane, precisely localizing the light field for each nanostructure.

On the other hand, nonradiative relaxation modes associated with localized surface plasmon resonances can directly induce the generation of hot carriers. In plasmonic nanostructures, when the excited state of plasmons interacts with other electrons or lattice vibrations, energy can be transferred to other electrons or lattice vibrations through nonradiative relaxation. Therefore, the combined effects of the aforementioned two aspects enable the hot electrons in Au nanostructures, acquiring additional energy from the LSPR effect and further augmenting the heating process. As nMAG has already undergone intrinsic hot-carrier effects, the introduction of localized surface plasmons initiates a heating process based on the further amplification of intrinsic hot carriers.

Furthermore, the Schottky barrier and the depletion region widths increase with electric field enhancement. The higher electrical field could improve the collection efficiency of electron–hole pairs (EHPs). Then the EHPs formed are collected within the depletion region of the junction and transported to the external circuit. Therefore, the strong electric field generated in the physically confined region of the nMAG–Au–Si structure, achieved through reverse bias voltage, is one of the mechanisms for efficient electron transport. This is due to the effective collection of multiple excited charge carriers prior to recombination, carrier scattering, and phonon dissipation. Thus, the intensified electric field enhances the electron transport efficiency within the device.

The photoresponse mechanism of the plasmon resonance-enhanced dual-band IR photodetector with hot carriers is depicted in Fig. 4(a). The absorption of incident photons occurs through Au nanostructures coupled with nMAG, generating electron-hole pairs. The SBH of 0.87 eV corresponds to a

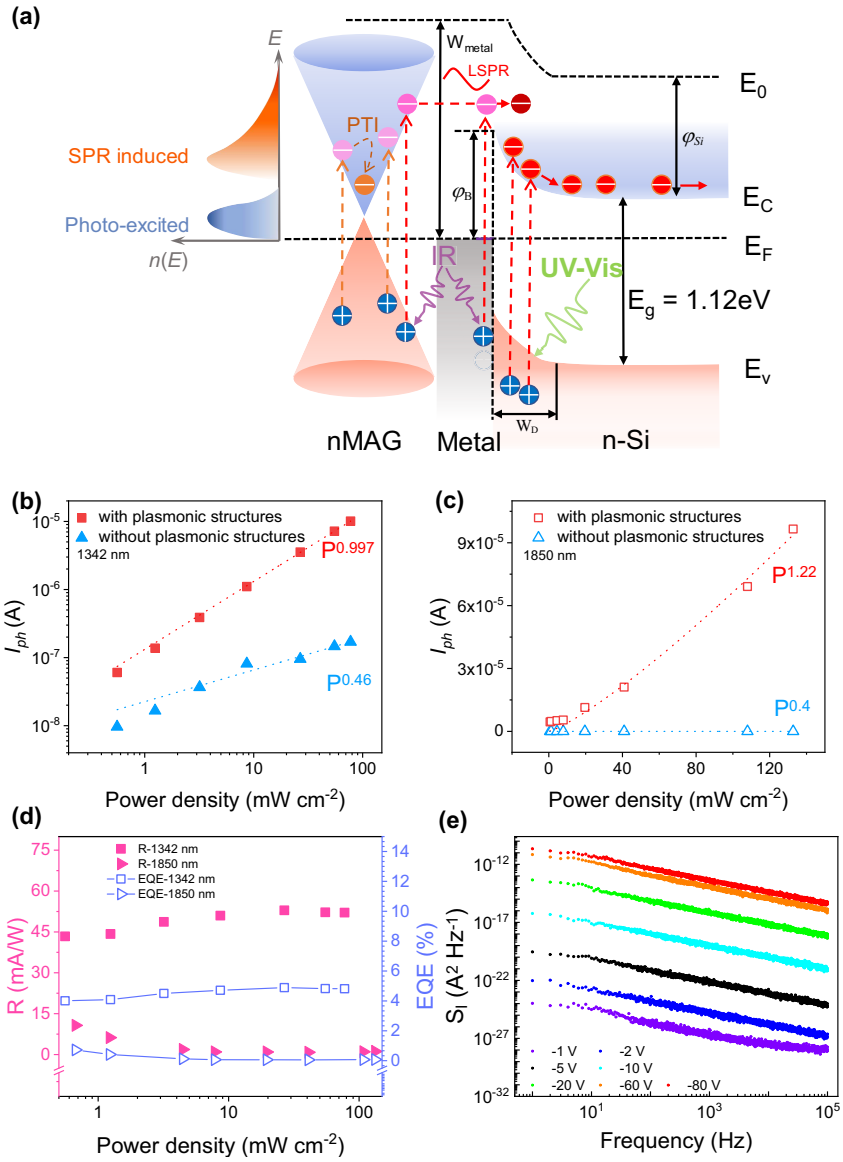

Fig. 4. Optoelectric characteristics of the plasmonic nanostructure-based photodetector with enhanced photoresponse. (a) The band diagram is associated with the hot-carrier generation by the PTI effect and SPR-induced process under infrared light optical excitation of the nMAG–Au–Si photodetector. (b), (c) Photocurrent as a function of different incident power densities with (red squares) and without (blue triangles) nanostructures under the bias of −1 V at the wavelengths of 1342 nm and 1850 nm, respectively. The data are fitted with a power law $I_{ph} \sim P^{\beta}$, and the corresponding fitting results were represented as dashed lines of the same color as the data sets. (d) Relationship between responsivity (pink scatter) and external quantum efficiency (EQE) (lavender line and scatter) under increasing power density at 1342 nm (squares) and 1850 nm (triangles). (e) Noise power spectral density (NSD) S_I of the nMAG–Au–Si vertical structure under various voltage bias conditions.

cut-off wavelength of 1425 nm. Therefore, when the photons with a wavelength ≤1.1 μm, such as ultraviolet and visible light, are absorbed by Si, this results in excited EHP in Si, which separates directly in the depletion region, producing a photocurrent. For photon energies $h\upsilon \geq$ SBH, the photoexcited electrons transport directly over the barrier and contribute to the photocurrent through the internal photoemission (IPE) effect.

When the incident wavelength exceeds 1425 nm, the energy of the optically excited electrons is lower than that of the SBH. Consequently, the photons cannot traverse the SBH directly but undergo thermalization. Partially thermally excited electrons, which possess energies higher than the SBH, can be emitted into the plasmonic nanostructure and Si through the PTI effect. Within this wavelength region, the portion of thermionic electrons in the Fermi–Dirac distribution of nMAG with energies higher than the SBH decreases with decreasing incident photon energy, thereby reducing responsivity [see Fig. 4(d)]. The photon-dominant mechanisms in the IPE and PTI effect enable the devices to undergo rapid dynamical processes.

To investigate the conduction characteristics of the device, the power-dependent photoresponse was examined, showcasing the photocurrent variation under different power

density conditions for illuminations at 1342 nm and 1850 nm [Figs. 4(b) and 4(c)]. The photocurrents are fitted with the power law $I_{ph} \sim P^{\beta}$, representing the exponent obtained from the fitting dashed line. In Fig. 4(b), the β value of 0.997 at 1342 nm displays the linear power dependence with the plasmonic structures, indicating a linear power dependence with the plasmonic structures, which suggests the occurrence of the IPE effect in the plasmonic structure coupled with nMAG. For the nMAG/Si heterojunction without plasmonic structures, the fitting curve yields a β value of 0.46. The sublinear relationship observed in the fitting curve arises due to the increased energy and power of the photon. This photocurrent saturation phenomenon at low power density means the EHP cannot separate efficiently in the device without a plasmonic structure.

Figure 4(c) shows a β value of 1.22 at 1850 nm with a clear superlinear power dependence. This is a typical feature of hot-carrier transport in graphene heterojunction devices [30]. This characteristic is a hallmark of the thermionic emission due to the generation of hot electrons from nMAG and plasmonic nanostructures. It also suggests the presence of the PTI effect in the device. Furthermore, for the device without plasmonic structures, β is fitted with a value of 0.4, indicating the current saturated at the wavelength of 1850 nm.

Therefore, the photocurrent of the plasmonic structures is more than one order higher than that without plasmonic structures. When the device is illuminated by incident light, two types of electrons are primarily generated. One is excited by photons, and the other is generated through surface plasmon resonance enhancement. After introducing Au plasmonic nanostructures, the device demonstrates distinct LSPR effects at approximately 1342 nm and 1850 nm. Upon irradiation of the device by incident light, first of all, nMAG will generate photo-induced hot carriers. This phenomenon arises from the intrinsic photo-induced hot-carrier effect of nMAG, where the high-energy electrons at the thermal distribution's tail possess higher energy than directly excited photoelectrons. However, limited absorption of nMAG results in lower thermalization efficiency, leading to a lower distribution of carriers in the high-energy region. Under the LSPR effect introduced by Au nanostructures, nMAG generates hot electrons through the intrinsic thermal carrier effect, which then vertically tunnel into the Au nanostructures. These tunneling electrons and the hot electrons at Au nanostructures' interfaces undergo further heating through nonradiative relaxation, giving rise to superhot electrons. Through the synergistic effect of the PTI effect and LSPR effect, the nMAG and Au nanostructure system can acquire more energy under the same illumination conditions, thereby allowing for a more substantial distribution of electrons in the high-energy state. The energy of these electrons far exceeds that of directly excited photoelectrons. Electrons distributed in the high-energy state, approaching or surpassing the barrier height, can traverse the barrier by applied voltage bias through thermal emission, subsequently entering the Si and generating photocurrent.

We calculated the responsivities $[R = (I_{ph} - I_{dark})P_{in}]$ to analyze the anticipated enhancement of responsivity resulting from the plasmonic nanostructure, as shown in Fig. 4(d). The responsivity is 52.9 mA/W on average at 1342 nm and 10.72 mA/W at 1850 nm. The discrepancy arises from the difference in absorbance between the two wavelengths. Additionally, the EQE can be determined by $\eta = R(hc/e\lambda)$. The maximum calculated responsivity and EQE are 19.82 A/W and 18.3% at 38 μW cm^{-2}, respectively.

Figure 4(e) illustrates the low-frequency noise density spectra. The device exhibits standard flicker noise, characterized by a nearly perfect $1/f$ spectrum, and shows relatively low noise power densities. This remarkable low-noise property of the dual-band plasmonic-enhanced photodetector holds great potential for improving sensitivity in IR photodetection applications.

The excited electrons will rapidly relax through interactions with electron–electron and electron–lattice processes. This change can be detected through the transient absorption of the material [62]. The Bernel stacking structure of nMAG enables strong electron–electron scattering and thus enhances the PTI effect [23]. The device system involves hot-carrier generation in Au, hot-carrier transfer between Au and graphene, and hot-carrier damping in Au and graphene. These complex processes have been expounded upon in the above discussion describing the device mechanism. To investigate the hot-carrier dynamics and track the state of hot electrons, we measured a pump-probe transient absorption (pump at 1550 nm and probe at 1.2–1.6 μm) of nMAG, as shown in Fig. 5(a). The normalized differential transmission $\Delta T/T_0$ in the figure

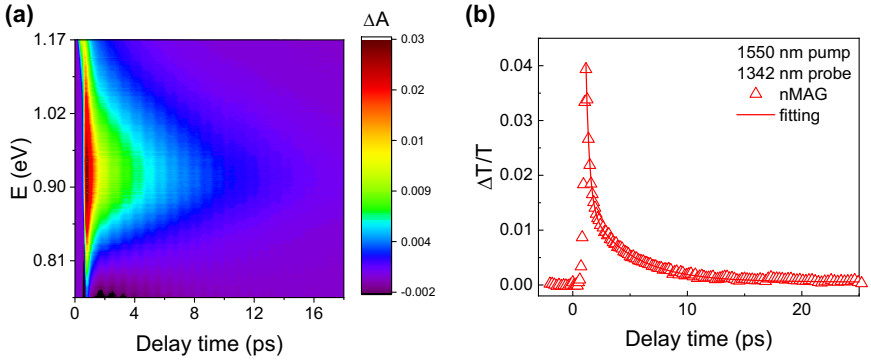

Fig. 5. Hot-carrier transport in nMAG. (a) 2D transient absorption mapping of nMAG on BaF_2 as functions of probe delay time and the incident photon energy. (b) Normalized differential transmittance of the sample under pump light of 1550 nm under 1 mW/mm^2. The signal was probed and collected at 1342 nm.

confirms that the pronounced occupation of strong orbits beyond the energy of incident photons signifies the robust PTI effect in nMAG. The total relaxation time of hot electrons in nMAG comprises thermalization and cooling. The thermalization time of hot electrons in nMAG is less than 500 fs. The cooling time is determined by electron–phonon scattering. The localization of states and the *E-k* relationship in nMAG result in weak electron–phonon interactions and limited energy transitions between electrons and phonons. With reduced electron–phonon interactions, certain electron–phonon energy transfer processes become prohibited, extending the thermal dissipation time from hot electrons to phonons. Consequently, the thermal phonon relaxation time is on the order of picoseconds (ps) in nMAG. The relaxation process of stimulated carriers follows a biexponential decay, and, by fitting the results, the carrier lifetime can be determined. The fitted biexponential decay curve in Fig. 3(f) shows that the carrier relaxation time in nMAG is approximately 4.9 ps. The longer relaxation time in nMAG implies less electron–phonon scattering and a more efficient electron transport pathway.

Therefore, the contribution of the plasmonic-induced light trapping and the enhanced electric field resulting from the LSPR effect and the strong PTI effect of nMAG collectively improve the device's photoresponse.

D. Transient Photoresponse of nMAG–Au–Si Nanostructure Photodetector

Benefitting from the low noise power spectral density of the dual-band plasmonic device, the NEP and D^* are calculated under 1342 nm illumination, as shown in Fig. 6(a). D^* is a critical factor corresponding to the sensitivity that can detect incident light by distinguishing noise signal [63], which can be extracted by $D^* = R\sqrt{A/(2eI_{\text{dark}})}$. A is the effective area of the device. At the same time, the NEP can be calculated by $\text{NEP} = S_n/R$ where $S_n = \sqrt{I^2_{\text{noise}}/1\ \text{Hz}} = \sqrt{S_I}$. The D^* and NEP can be extracted as 4.77×10^{10} Jones and 2.10×10^{-11} $\text{W/Hz}^{1/2}$.

Figure 6(b) depicts the normalized photoresponse of the photodetector as the modulated frequency varies from 1 Hz to 500 kHz, allowing for the estimation of a –3 dB bandwidth of 290 kHz. In Fig. 6(c), a periodic response is observed at a power density of 200 mW cm^{-2} with a frequency of 100 kHz under 1342 nm illumination. The rising time (τ_r) and falling time (τ_f) are estimated as 712 ns and 1.76 µs, comparable to other infrared photodetectors. Figure 6(d) illustrates the photocurrent response under different power densities using a modulated 1342 nm laser frequency of 100 kHz. The response speed can be enhanced by optimizing the interface quality during etching and reducing the parasitic time constant of the external circuits.

4. CONCLUSION

In conclusion, we have demonstrated a new concept for dual-band IR silicon photodetectors based on the coupling of nMAG devices with metallic plasmonic nanostructures. This coupling enhances the local optical field by leveraging the high carrier density (1350 $\text{cm}^2\,\text{V}^{-1}\,\text{s}^{-1}$) and long carrier relaxation

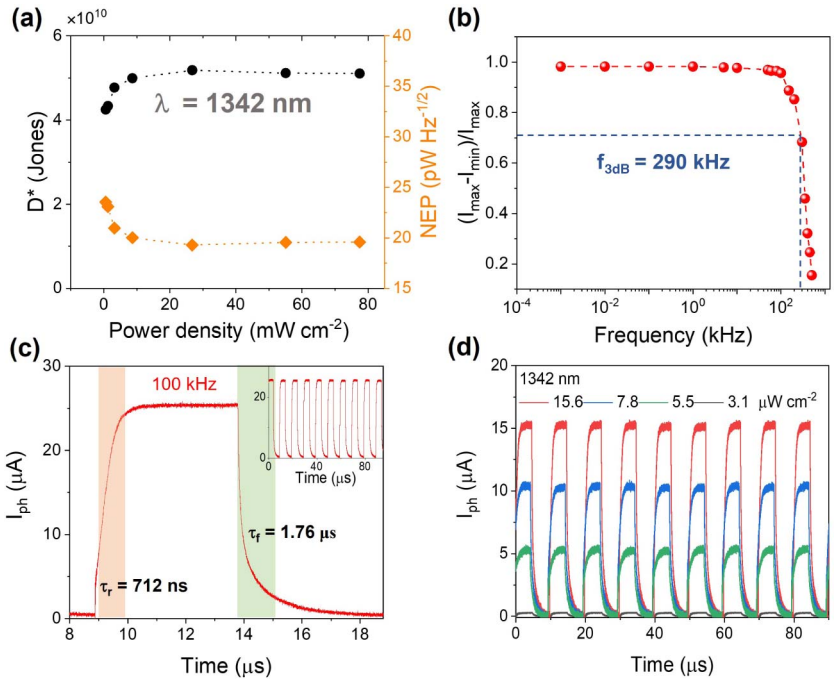

Fig. 6. Specific detectivity (D^*) and transient response time of the nanostructure photodetector. (a) D^* and noise-equivalent-power (NEP) as a function of the varying power density under the illumination of 1342 nm. (b) Normalized photoresponse under the different frequencies from 1 Hz to 500 kHz illuminated with the CW 1342 nm laser capable of TTL on/off modulation, indicating the –3 dB bandwidth of 290 kHz. (c) Rising and falling times are obtained from the inset: time-dependent photocurrent of the device with a power density of 200 mW cm^{-2} with the frequency of 100 kHz under the illumination of 1342 nm. The response times are extracted within the photocurrent level of 10%–90%. (d) Photoresponse of the device with varying power conditions under 1342 nm laser modulated by the frequency of 100 kHz.

time (4.9 ps) of nMAG, resulting in a remarkable plasmonic response enhancement of more than a factor of 10. The plasmonic structure we have designed exhibits two resonant absorption peaks in the infrared spectrum at 1342 nm and 1850 nm. Additionally, owing to the Schottky barrier of the device, the nMAG–Au–Si device exhibits IPE and PTI effects in the photoresponse at the wavelengths of 1342 nm and 1850 nm, respectively. The combination of plasmonic-induced light trapping and plasmonic-enhanced hot electron injection, through nMAG and nanostructure, proves strong carrier multiplication with a responsivity of 52.9 mA/W and D^* of 4.77×10^{10} Jones. Our findings present a practical approach for detecting low-energy photons and enhancing photoresponse in IR optoelectronic applications. Furthermore, the integration SPR silicon nanostructure with nMAG opens up a promising pathway for generating, harnessing, and manipulating hot carriers.

Funding. Natural Science Foundation of Zhejiang Province (LDT23F04013F04); Fundamental Research Funds for the Central Universities (2021FZZX001-17); National Natural Science Foundation of China (62090034, 92164106, U22A2076).

Acknowledgment. The work is supported by Zhejiang University (ZJU) Micro-Nano Fabrication Center. The authors thank Prof. Yuda Zhao and Liying Chen for their valuable experimental support and comments. This work is led jointly by Prof. Li Peng, Prof. Huan Hu, and Prof. Yang Xu.

Disclosures. The authors declare no conflicts of interest.

Data Availability. Data underlying the results presented in this paper are not publicly available at this time but may be obtained from the authors upon reasonable request.

REFERENCES

1. S. J. Haigh, A. Gholinia, R. Jalil, S. Romani, L. Britnell, D. C. Elias, K. S. Novoselov, L. A. Ponomarenko, A. K. Geim, and R. Gorbachev, "Cross-sectional imaging of individual layers and buried interfaces of graphene-based heterostructures and superlattices," Nat. Mater. **11**, 764–767 (2012).
2. H. Wang, H. S. Wang, C. Ma, L. Chen, C. Jiang, C. Chen, X. Xie, A.-P. Li, and X. Wang, "Graphene nanoribbons for quantum electronics," Nat. Rev. Phys. **3**, 791–802 (2021).
3. A. K. Geim and K. S. Novoselov, "The rise of graphene," Nat. Mater. **6**, 183–191 (2007).
4. T. Jiang, V. Kravtsov, M. Tokman, A. Belyanin, and M. B. Raschke, "Ultrafast coherent nonlinear nanooptics and nanoimaging of graphene," Nat. Nanotechnol. **14**, 838–843 (2019).
5. T. Tan, Z. Yuan, H. Zhang, G. Yan, S. Zhou, N. An, B. Peng, G. Soavi, Y. Rao, and B. Yao, "Multispecies and individual gas molecule detection using Stokes solitons in a graphene over-modal microresonator," Nat. Commun. **12**, 6716 (2021).
6. S. K. Behura, C. Wang, Y. Wen, and V. Berry, "Graphene–semiconductor heterojunction sheds light on emerging photovoltaics," Nat. Photonics **13**, 312–318 (2019).
7. Y. Xu, K. Shehzad, S. C. Bodepudi, A. Imran, and B. Yu, *Graphene for Post-Moore Silicon Optoelectronics* (Wiley, 2023).
8. D. Akinwande, C. Huyghebaert, C.-H. Wang, M. I. Serna, S. Goossens, L.-J. Li, H.-S. P. Wong, and F. H. L. Koppens, "Graphene and two-dimensional materials for silicon technology," Nature **573**, 507–518 (2019).
9. K. S. Novoselov, V. I. Fal'ko, L. Colombo, P. R. Gellert, M. G. Schwab, and K. Kim, "A roadmap for graphene," Nature **490**, 192–200 (2012).
10. B. Sun, R. N. McCay, S. Goswami, Y. Xu, C. Zhang, Y. Ling, J. Lin, and Z. Yan, "Gas-permeable, multifunctional on-skin electronics based on laser-induced porous graphene and sugar-templated elastomer sponges," Adv. Mater. **30**, 1804327 (2018).
11. R. You, Y.-Q. Liu, Y.-L. Hao, D.-D. Han, Y.-L. Zhang, and Z. You, "Laser fabrication of graphene-based flexible electronics," Adv. Mater. **32**, 1901981 (2020).
12. E. O. Polat, G. Mercier, I. Nikitskiy, E. Puma, T. Galan, S. Gupta, M. Montagut, J. J. Piqueras, M. Bouwens, T. Durduran, G. Konstantatos, S. Goossens, and F. Koppens, "Flexible graphene photodetectors for wearable fitness monitoring," Sci. Adv. **5**, eaaw7846 (2019).
13. Z. Lou, L. Zeng, Y. Wang, D. Wu, T. Xu, Z. Shi, Y. Tian, X. Li, and Y. H. Tsang, "High-performance MoS_2/Si heterojunction broadband photodetectors from deep ultraviolet to near infrared," Opt. Lett. **42**, 3335–3338 (2017).
14. M. Shimatani, N. Yamada, S. Fukushima, S. Okuda, S. Ogawa, T. Ikuta, and K. Maehashi, "High-responsivity turbostratic stacked graphene photodetectors using enhanced photogating," Appl. Phys. Express **12**, 122010 (2019).
15. J. Wei, Y. Li, L. Wang, W. Liao, B. Dong, C. Xu, C. Zhu, K.-W. Ang, C.-W. Qiu, and C. Lee, "Zero-bias mid-infrared graphene photodetectors with bulk photoresponse and calibration-free polarization detection," Nat. Commun. **11**, 6404 (2020).
16. W. Liu, J. Lv, L. Peng, H. Guo, C. Liu, Y. Liu, W. Li, L. Li, L. Liu, P. Wang, S. C. Bodepudi, K. Shehzad, G. Hu, K. Liu, Z. Sun, T. Hasan, Y. Xu, X. Wang, C. Gao, B. Yu, and X. Duan, "Graphene charge-injection photodetectors," Nat. Electron. **5**, 281–288 (2022).
17. J. Lv, Y. Dong, X. Cao, X. Liu, L. Li, W. Liu, H. Guo, X. Wang, S. C. Bodepudi, Y. Zhao, Y. Xu, and B. Yu, "Broadband graphene field-effect coupled detectors: from soft X-ray to near-infrared," IEEE Electron Device Lett. **43**, 902–905 (2022).
18. X. Liu, H. Ning, J. Lv, L. Liu, L. Peng, F. Tian, S. C. Bodepudi, X. Wang, X. Cao, Y. Dong, W. Fang, S. Wu, H. Hu, B. Yu, and Y. Xu, "High-performance broadband graphene/silicon/graphene photodetectors: from X-ray to near-infrared," Appl. Phys. Lett. **122**, 071105 (2023).
19. M. S. Choi, A. Nipane, B. S. Y. Kim, M. E. Ziffer, I. Datta, A. Borah, Y. Jung, B. Kim, D. Rhodes, A. Jindal, Z. A. Lamport, M. Lee, A. Zangiabadi, M. N. Nair, T. Taniguchi, K. Watanabe, I. Kymissis, A. N. Pasupathy, M. Lipson, X. Zhu, W. J. Yoo, J. Hone, and J. T. Teherani, "High carrier mobility in graphene doped using a monolayer of tungsten oxyselenide," Nat. Electron. **4**, 731–739 (2021).
20. J. H. Gosling, O. Makarovsky, F. Wang, N. D. Cottam, M. T. Greenaway, A. Patanè, R. D. Wildman, C. J. Tuck, L. Turyanska, and T. M. Fromhold, "Universal mobility characteristics of graphene originating from charge scattering by ionised impurities," Commun. Phys. **4**, 30 (2021).
21. L. Yang, J. Deslippe, C.-H. Park, M. L. Cohen, and S. G. Louie, "Excitonic effects on the optical response of graphene and bilayer graphene," Phys. Rev. Lett. **103**, 186802 (2009).
22. S. M. Koepfli, M. Baumann, Y. Koyaz, R. Gadola, A. Güngör, K. Keller, Y. Horst, S. Nashashibi, R. Schwanninger, M. Doderer, E. Passerini, Y. Fedoryshyn, and J. Leuthold, "Metamaterial graphene photodetector with bandwidth exceeding 500 gigahertz," Science **380**, 1169–1174 (2023).
23. D. Brida, A. Tomadin, C. Manzoni, Y. J. Kim, A. Lombardo, S. Milana, R. R. Nair, K. S. Novoselov, A. C. Ferrari, G. Cerullo, and M. Polini, "Ultrafast collinear scattering and carrier multiplication in graphene," Nat. Commun. **4**, 1987 (2013).
24. K. J. Tielrooij, J. C. W. Song, S. A. Jensen, A. Centeno, A. Pesquera, A. Zurutuza Elorza, M. Bonn, L. S. Levitov, and F. H. L. Koppens, "Photoexcitation cascade and multiple hot-carrier generation in graphene," Nat. Phys. **9**, 248–252 (2013).
25. X. Lu, L. Sun, P. Jiang, and X. Bao, "Progress of photodetectors based on the photothermoelectric effect," Adv. Mater. **31**, 1902044 (2019).
26. K. J. Tielrooij, L. Piatkowski, M. Massicotte, A. Woessner, Q. Ma, Y. Lee, K. S. Myhro, C. N. Lau, P. Jarillo-Herrero, N. F. van Hulst, and

F. H. L. Koppens, "Generation of photovoltage in graphene on a femtosecond timescale through efficient carrier heating," Nat. Nanotechnol. **10**, 437–443 (2015).
27. Q. Ma, N. M. Gabor, T. I. Andersen, N. L. Nair, K. Watanabe, T. Taniguchi, and P. Jarillo-Herrero, "Competing channels for hot-electron cooling in graphene," Phys. Rev. Lett. **112**, 247401 (2014).
28. N. M. Gabor, J. C. W. Song, Q. Ma, N. L. Nair, T. Taychatanapat, K. Watanabe, T. Taniguchi, L. S. Levitov, and P. Jarillo-Herrero, "Hot carrier–assisted intrinsic photoresponse in graphene," Science **334**, 648–652 (2011).
29. K. K. Paul, J.-H. Kim, and Y. H. Lee, "Hot carrier photovoltaics in van der Waals heterostructures," Nat. Rev. Phys. **3**, 178–192 (2021).
30. Q. Ma, T. I. Andersen, N. L. Nair, N. M. Gabor, M. Massicotte, C. H. Lui, A. F. Young, W. Fang, K. Watanabe, T. Taniguchi, J. Kong, N. Gedik, F. H. L. Koppens, and P. Jarillo-Herrero, "Tuning ultrafast electron thermalization pathways in a van der Waals heterostructure," Nat. Phys. **12**, 455–459 (2016).
31. Y. Lin, Q. Ma, P.-C. Shen, B. Ilyas, Y. Bie, A. Liao, E. Ergeçen, B. Han, N. Mao, X. Zhang, X. Ji, Y. Zhang, J. Yin, S. Huang, M. Dresselhaus, N. Gedik, P. Jarillo-Herrero, X. Ling, J. Kong, and T. Palacios, "Asymmetric hot-carrier thermalization and broadband photoresponse in graphene-2D semiconductor lateral heterojunctions," Sci. Adv. **5**, eaav1493 (2019).
32. S. Fu, I. du Fossé, X. Jia, J. Xu, X. Yu, H. Zhang, W. Zheng, S. Krasel, Z. Chen, Z. M. Wang, K.-J. Tielrooij, M. Bonn, A. J. Houtepen, and H. I. Wang, "Long-lived charge separation following pump-wavelength–dependent ultrafast charge transfer in graphene/WS_2 heterostructures," Sci. Adv. **7**, eabd9061 (2021).
33. R. R. Nair, P. Blake, A. N. Grigorenko, K. S. Novoselov, T. J. Booth, T. Stauber, N. M. R. Peres, and A. K. Geim, "Fine structure constant defines visual transparency of graphene," Science **320**, 1308 (2008).
34. V. G. Kravets, A. N. Grigorenko, R. R. Nair, P. Blake, S. Anissimova, K. S. Novoselov, and A. K. Geim, "Spectroscopic ellipsometry of graphene and an exciton-shifted van Hove peak in absorption," Phys. Rev. B **81**, 155413 (2010).
35. L. Peng, Y. Han, M. Wang, X. Cao, J. Gao, Y. Liu, X. Chen, B. Wang, B. Wang, C. Zhu, X. Wang, K. Cao, M. Huang, B. V. Cunning, J. Pang, W. Xu, Y. Ying, Z. Xu, W. Fang, Y. Lu, R. S. Ruoff, and C. Gao, "Multifunctional macroassembled graphene nanofilms with high crystallinity," Adv. Mater. **33**, 2104195 (2021).
36. L. Peng, L. Liu, S. Du, S. C. Bodepudi, L. Li, W. Liu, R. Lai, X. Cao, W. Fang, Y. Liu, X. Liu, J. Lv, M. Abid, J. Liu, S. Jin, K. Wu, M. Lin, X. Cong, P. Tan, H. Zhu, Q. Xiong, X. Wang, W. Hu, X. Duan, B. Yu, Z. Xu, Y. Xu, and C. Gao, "Macroscopic assembled graphene nanofilms based room temperature ultrafast mid-infrared photodetectors," InfoMat **4**, e12309 (2022).
37. L. Liu, X. Cao, L. Peng, S. C. Bodepudi, S. Wu, W. Fang, J. Liu, Y. Xiao, X. Wang, Z. Di, R. Cheng, Y. Xu, C. Gao, and B. Yu, "Macroscopic-assembled-graphene nanofilms/germanium broadband photodetectors," in *IEEE International Electron Devices Meeting (IEDM)* (2021), pp. 9.2.1–9.2.4.
38. M. W. Knight, H. Sobhani, P. Nordlander, and N. J. Halas, "Photodetection with active optical antennas," Science **332**, 702–704 (2011).
39. M. Kim, J.-H. Lee, and J.-M. Nam, "Plasmonic photothermal nanoparticles for biomedical applications," Adv. Sci. **6**, 1900471 (2019).
40. S. S. Aćimović, H. Šípová, G. Emilsson, A. B. Dahlin, T. J. Antosiewicz, and M. Käll, "Superior LSPR substrates based on electromagnetic decoupling for on-a-chip high-throughput label-free biosensing," Light Sci. Appl. **6**, e17042 (2017).
41. O. Zandi, A. Agrawal, A. B. Shearer, L. C. Reimnitz, C. J. Dahlman, C. M. Staller, and D. J. Milliron, "Impacts of surface depletion on the plasmonic properties of doped semiconductor nanocrystals," Nat. Mater. **17**, 710–717 (2018).
42. X. Sun, H. Liu, L. Jiang, R. Wei, C. Wang, X. Wang, X. Sun, F. Wang, X. Lu, A. B. Evlyukhin, and C. Huang, "Directional surface plasmon polariton scattering by single low-index dielectric nanoparticles: simulation and experiment," Photon. Res. **11**, 765–772 (2023).
43. K. Wu, J. Chen, J. R. McBride, and T. Lian, "Efficient hot-electron transfer by a plasmon-induced interfacial charge-transfer transition," Science **349**, 632–635 (2015).
44. C. Clavero, "Plasmon-induced hot-electron generation at nanoparticle/metal-oxide interfaces for photovoltaic and photocatalytic devices," Nat. Photonics **8**, 95–103 (2014).
45. J. Tong, F. Suo, J. Ma, L. Y. Tobing, L. Qian, and D. H. Zhang, "Surface plasmon enhanced infrared photodetection," Opto-Electron. Adv. **2**, 18002601 (2019).
46. M. L. Brongersma, N. J. Halas, and P. Nordlander, "Plasmon-induced hot carrier science and technology," Nat. Nanotechnol. **10**, 25–34 (2015).
47. Z. Chen, X. Li, J. Wang, L. Tao, M. Long, S.-J. Liang, L. K. Ang, C. Shu, H. K. Tsang, and J.-B. Xu, "Synergistic effects of plasmonics and electron trapping in graphene short-wave infrared photodetectors with ultrahigh responsivity," ACS Nano **11**, 430–437 (2017).
48. I. Vangelidis, D. V. Bellas, S. Suckow, G. Dabos, S. Castilla, F. H. L. Koppens, A. C. Ferrari, N. Pleros, and E. Lidorikis, "Unbiased plasmonic-assisted integrated graphene photodetectors," ACS Photon. **9**, 1992–2007 (2022).
49. B. Wang, X. Zhang, F. J. García-Vidal, X. Yuan, and J. Teng, "Strong coupling of surface plasmon polaritons in monolayer graphene sheet arrays," Phys. Rev. Lett. **109**, 073901 (2012).
50. L.-B. Luo, L.-H. Zeng, C. Xie, Y.-Q. Yu, F.-X. Liang, C.-Y. Wu, L. Wang, and J.-G. Hu, "Light trapping and surface plasmon enhanced high-performance NIR photodetector," Sci. Rep. **4**, 3914 (2014).
51. L. Scriven and C. Sternling, "The marangoni effects," Nature **187**, 186–188 (1960).
52. P. Gao, J. He, S. Zhou, X. Yang, S. Li, J. Sheng, D. Wang, T. Yu, J. Ye, and Y. Cui, "Large-area nanosphere self-assembly by a micropropulsive injection method for high throughput periodic surface nanotexturing," Nano Lett. **15**, 4591–4598 (2015).
53. S. Wu, C. Chen, X. Wu, F. Tian, Y. Ma, Y. Xu, and H. Hu, "Wafer-scale low-cost complementary vertically coupled plasmonic structure for surface-enhanced infrared absorption," Sens. Actuators B **382**, 133560 (2023).
54. B. Shan, L. Xia, S. Ma, Z. Yin, X. Liu, G. Li, and Y. Huang, "Achieving multiband compatible and mechanical tuning absorber using edge topological defect-induced graphene plasmon," Carbon **192**, 1–13 (2022).
55. X. Wan, Y. Xu, H. Guo, K. Shehzad, A. Ali, Y. Liu, J. Yang, D. Dai, C.-T. Lin, L. Liu, H.-C. Cheng, F. Wang, X. Wang, H. Lu, W. Hu, X. Pi, Y. Dan, J. Luo, T. Hasan, X. Duan, X. Li, J. Xu, D. Yang, T. Ren, and B. Yu, "A self-powered high-performance graphene/silicon ultraviolet photodetector with ultra-shallow junction: breaking the limit of silicon?" npj 2D Mater. Appl. **1**, 4 (2017).
56. Y. Xu, C. Cheng, S. Du, J. Yang, B. Yu, J. Luo, W. Yin, E. Li, S. Dong, P. Ye, and X. Duan, "Contacts between two- and three-dimensional materials: Ohmic, Schottky, and p–n heterojunctions," ACS Nano **10**, 4895–4919 (2016).
57. X. Li, D. Xiao, and Z. Zhang, "Landau damping of quantum plasmons in metal nanostructures," New J. Phys. **15**, 023011 (2013).
58. A. Manjavacas, J. G. Liu, V. Kulkarni, and P. Nordlander, "Plasmon-induced hot carriers in metallic nanoparticles," ACS Nano **8**, 7630–7638 (2014).
59. E. Kazuma, J. Jung, H. Ueba, M. Trenary, and Y. Kim, "Real-space and real-time observation of a plasmon-induced chemical reaction of a single molecule," Science **360**, 521–526 (2018).
60. Y. Liu, R. Cheng, L. Liao, H. Zhou, J. Bai, G. Liu, L. Liu, Y. Huang, and X. Duan, "Plasmon resonance enhanced multicolour photodetection by graphene," Nat. Commun. **2**, 579 (2011).
61. A. Zada, P. Muhammad, W. Ahmad, Z. Hussain, S. Ali, M. Khan, Q. Khan, and M. Maqbool, "Surface plasmonic-assisted photocatalysis and optoelectronic devices with noble metal nanocrystals: design, synthesis, and applications," Adv. Funct. Mater. **30**, 1906744 (2020).
62. Y. Yang, J. Gu, J. L. Young, E. M. Miller, J. A. Turner, N. R. Neale, and M. C. Beard, "Semiconductor interfacial carrier dynamics via photoinduced electric fields," Science **350**, 1061–1065 (2015).
63. Y. Fang, A. Armin, P. Meredith, and J. Huang, "Accurate characterization of next-generation thin-film photodetectors," Nat. Photonics **13**, 1–4 (2019).